5-2014

Land Cover Change and its Impacts on a Flash Flood-Producing Rain Event in Eastern Kentucky

William N. Rodgers
Western Kentucky University, william.rodgers@wku.edu

LAND COVER CHANGE AND ITS IMPACTS ON A FLASH FLOOD-PRODUCING RAIN EVENT IN EASTERN KENTUCKY

A Thesis
Presented to
The Faculty of the Department of Geography and Geology
Western Kentucky University
Bowling Green, Kentucky

In Partial Fulfillment
of the Requirements for the Degree
Master of Science

By
William Rodgers

May 2014

LAND COVER CHANGE AND ITS IMPACTS ON A FLASH FLOOD PRODUCING RAIN EVENT IN EASTERN KENTUCKY

Date Recommended 04/11/14

Rezaul Mahmood, Director of Thesis

Stuart Foster

Jun Yan

Dean, Graduate Studies and Research 5-5-14 Date

ACKNOWLEDGEMENTS

This research started by an interest in flash flooding from Dr. Rezaul Mahmood. He offered me an opportunity for a research position, when, at the time, all I was trying to do was say hello to a former professor. The initial funding was provided by the Kentucky Climate Center and the Department of Geography and Geology. This paved the way for the development of a flash flood database for eastern Kentucky from 1993-2005. Then Dr. Mahmood was able to secure a grant through NCDC, which funded my research to include not only eastern Kentucky from 1978-2005 but also 295 counties of Appalachia.

Afterwards, Dr. Mahmood introduced me to Ronnie Leeper and, eventually, Dr. Arturo Quintanar. It was through Ronnie Leeper's efforts that I learned how to use the Weather Research and Forcasting (WRF) model and to modify it. It was also through Dr. Quitnanar's efforts that I learned the necessary Fortran programming language to understand the WRF program and how to modify it efficiently.

Also during my tenure, I was introduced to Geographic Information Systems (GIS). I thank those in the Department of Geography and Geology who made Foundations of GIS a program requirement, otherwise I would not have found a field of study and analysis of which I am now quite fond. I would also like to thank Mr. Scott Dobler, Dr. Katie Algeo, Dr. Jun Yan, and Mr. Kevin Cary for the knowledge, the tools, and the encouragement to understand more fully the field of Geographic Information Science and to utilize the tool that is GIS.

I would also like to thank Wendy Decroix for all her assistance, and especially her patience. I would also like to thank Dr. Stuart Foster and Dr. David Keeling for their

guidance and assistance through the years. I am grateful for the support of my family, as well as the ongoing encouragement of my girlfriend, Ms. Rachel Lynne Green, that has helped me finish this stretch of the marathon of life.

Table of Contents

List of Figures

List of Tables

LAND COVER CHANGE AND ITS IMPACTS ON A FLASH FLOOD-PRODUCING RAIN EVENT IN EASTERN KENTUCKY

William Rodgers May 2014 75 Pages

Directed by: Rezaul Mahmood, Stuart Foster, and Jun Yan

Department of Geography and Geology Western Kentucky University

Eastern Kentucky is a 35-county region that is a part of the Cumberland Plateau of the Appalachian Mountains. With mountaintop removal and associated land cover change (LCC) (primarily deforestation), it is hypothesized that there would be changes in various atmospheric boundary layer parameters and precipitation. In this research, we have conducted sensitivity experiments of atmospheric response of a significant flash flood-producing rainfall event by modifying land cover and topography. These reflect recent LCC, including mountaintop removal (MTR). We have used the Weather Research and Forecasting (WRF) model for this purpose. The study found changes in amount, location, and timing of precipitation. LCC also modified various surface fluxes, moist static energy, planetary boundary layer height, and local-scale circulation wind circulation.

The key findings were the modification in fluxes and precipitation totals. With respect to sensible heat flux (*H*), there was an increase to bare soil (post-MTR) in comparison to pre-MTR conditions (increased elevation with no altered land cover). Allowing for growth of vegetation, the grass simulation resulted in a decrease in *H*. *H* increased when permitting the growth of forest land cover (LC) but not to the degree of bare soil. In regards to latent heat flux (*LE*), there was a dramatic decrease transitioning from pre-MTR to post-MTR simulations. Then with the subsequent grass and forest simulations, there was an increase in *LE* comparable to the pre-MTR simulation. Under

pre-MTR conditions, the total precipitation was at its highest level overall. Then with the simulated loss of vegetation and elevation, there was a dramatic decrease in precipitation. With the grass LC, the precipitation increased in all areas of interest. Then forest LC was simulated allowing overall slightly higher precipitation than grass.

Chapter 1

Introduction

Land cover plays an important role in land surface atmosphere interactions, including evapotranspiration, low level turbulence and transport, convection, precipitation, infiltration, soil water holding capacity, and runoff (Matthews et al., 2003; Narisma and Pitman, 2003; Adegoke et al., 2007; Schneider and Eugster, 2005; Gero et al., 2006; Eastman et al., 2001; Pitman et al., 2004). Hence, land cover change (LCC) further affects these relationships.

LCC impacts albedo, vegetation fraction and, thereby, radiation and energy partitioning (Pielke et al., 2007; Matthews et al., 2003; Gero et al., 2006; Adegoke et al., 2007; Narisma and Pitman, 2003). LCC also changes the leaf area index (LAI) and associated stomatal regulation of plant transpiration (Eastman et al., 2001; Matthews et al., 2003; Narisma and Pitman, 2003; Gero et al., 2006; Adegoke et al., 2007; Siqueira et al., 2009). Moreover, LCC modifies canopy height and thus changes air flow, eddies, turbulences, moisture and energy transfer (Narisma and Pitman, 2003; Pitman et al., 2004; Gero et al., 2006; Adegoke et al., 2007; Siqueira et al., 2009). Turbulence leads to mixing of the planetary boundary layer, which may lead to enhancement of vertical motion, depending on moisture availability (Narisma and Pitman, 2003; Schneider and Eugster, 2005; Gero et al., 2006; Adegoke et al., 2007). LCC impacts moisture availability in the atmosphere by modifying evapotranspiration, which is partly dependent on vegetation type and related root system (Matthews et al., 2003; Oke, 1987; Siqueira et al., 2009).

These changes impact the boundary layer (Gero et al., 2006; Adegoke et al., 2007; Narisma and Pitman, 2003). Schneider and Eugster (2005) noted that these changes resulted in alterations with respect to daytime mixing, convection and cloud cover. Pitman et al. (2004) found that LCC and related altered surface roughness affected turbulence of the boundary layer, impacting moisture convergence and then temperature and precipitation. Eastman et al. (2001) investigated the impacts of grazing on the regional climate of the Great Plains. With the absence of grazing, there was an increase of evapotranspiration allowing for higher latent heat flux (*LE*) and thus lowered sensible heat flux (*H*). The lowering of the *H* resulted in cooler temperatures and a smaller diurnal temperature range. However, Eastman et al. (2001) did suggest the possibility of lowering of LCC impacts under synoptic-scale transport of moisture, which would over-ride local evapotranspiration.

Recently, Loveland and Acevedo (2012) analyzed LCC from 1973 to 2000 for the U.S. The purpose was to characterize the location of the change, changes in land cover types, the types of modification, the rates of LCC, and the causes of changes. Their study was conducted using probability sampling, satellite imaging, and aerial photography. As part of the research they divided the U. S. into a number of regions and ecoregions. The ecoregions were designated via geographic contiguity and similar characteristics such as climate, vegetation, topography, and soils. In the Eastern U.S., there are 20 ecoregions covering 165 million square kilometers. Of this region, almost 21 million square kilometers have experienced some level of LCC over the 27-year period.

Eastern Kentucky has three of these ecoregions, including the Southwestern Appalachians, the Central Appalachians, and the Western Allegheny Plateau. Sohl

(2012) noted that, during 1973 to 2000, 16 percent of the LCC over the southwestern Appalachians was directly related to mining. In the Central Appalachians and the Western Allegheny Plateau, mining was involved in 57 and 30 percent of the LCCs, respectively (Sayler, 2012a,b). Surface mining in the Appalachian Region has occurred since the 1930s, over an expanse of 1.8 million ha. (Demchak et al., 2004). Surface mining usually occurs in three phases. The first phase involves the removal of the vegetation and upper level soils and subsequent storage. The second phase removes the overbearing rock and mines the coal, before the overbearing rock is restored to approximate the original contours. Finally, in the third phase, the stored soil is placed on the surface and then seeded (Simmons et al., 2008).

In the 1970s, Mountaintop Removal (MTR) became prominent in the region (Fox, 1999). MTR, a type of surface mining, can potentially require the removal of 152 m (~500 ft) or more of the land surface (Fox, 1999). The removed material is then typically deposited into nearby valleys, impacting any associated headwaters, primarily with respect to water quality (Hartman et al., 2005). Philips (2004) has investigated the potential impacts of valley fills on flash flooding. The research was inconclusive due to uncertainties in the hydrological conditions. In the restoration process, the soil is compacted and of poor quality, which may prevent forest development for a period of 150 to 200 years allowing growth for primarily grasses and shrubs (Fox, 1999; Simmons et al., 2008). Holl (2002) mentions the lack of fulfillment with respect to land cover restoration as part of post-MTR. Currently, the focus is on short-term reclamation by any vegetation instead of a full restoration of the original vegetation types. According to Holl (2002), if done properly, the process of restoration would take 35 years or possibly more.

This process would include the use of native seeds with a wider variety of tree species. In addition, there is another potential option for establishment of more prevalent forest development in former MTR sites, through the work of hybridization of the Chinese and American Chestnut, which have been shown in some instances to be able to grow in soils of post-MTR (Skousen et al., 2013).

In this context, the purpose of this research is to understand the impacts of LCC on flash flood-producing heavy rainfall in Eastern Kentucky. To meet this goal, we have conducted sensitivity experiments via the Weather Research Forecasting model (WRF). The implantation of the WRF involved the use of the original LC as well as potential new LC, such as bare soil, grass, and forest. Due to the presence of MTR in Eastern Kentucky, the impacts of topography were also considered during the progression of this research. However, unlike Phillips (2004), this research only evaluated the implications of LCC and the affected meteorological conditions and did not delve into the surface hydrological impacts.

Chapter 2

Methodology

2.1. WRF Model Applications

For this study, the WRF version 3.2 was coupled to the WRF Single Moment 3 class microphysics (Hong and Lim, 2006), RRTM (Rapid Radiative Transfer Model) longwave radiation physics (Clough et al., 2005), Dudhia shortwave radiation physics (Chen and Dudhia, 2000), Eta surface layer physics (Tanny et al., 2008; Wang et al., 2010), NOAH LSM (Pan and Mahrt, 1987; Sridhar et al., 2002; Velde et al., 2009), Younsei University PBL scheme (Hu et al., 2010), and Kain-Fritsch cumulus parameterization scheme (Kain, 2004). The WRF Single Moment 3 microphysics uses simple ice and snow processes involving water vapor, cloud water and ice, and then rain/snow (Hong, 2006). RRTM takes into account multiple bands of radiation and trace gasses (Clough et al., 2005). The Dudhia scheme is a simple representation of cloud and clear-sky absorption and scattering of downward radiation (Chen and Dudhia, 2000), while Eta is based on the Momin-Obukhov theory involving the interaction of the land surface and the lower part of the planet boundary layer (Wang et al., 2010; Tanny et al., 2008). Noah LSM, formally known as OSU LSM (Oregon State University Land Surface Model), was originally developed by Pan and Mahrt (1987), and then renamed after a gradual revision by NCEP (Sridhar et al., 2002; Velde et al., 2009). Noah is composed of a single canopy layer with four soil layers. The surface model takes into consideration soil moisture via a reservoir and gravity drainage in the lower layer of soil. Noah involves the distribution of soil temperature and moisture across four layers and

incorporates snow cover and frozen soil as well as vegetation effects and subgrid variability (Sridhar et al., 2002).

The WRF simulation involved two domains with the outer domain 1932 km by 1692 km at12 km horizontal resolution centered at 40.0N and 86.0W (Figure 2.1). The inner domain's dimensions were 1203 km by 1023 km for a 3 km horizontal resolution and off-set from the outer domain by 360 km to the east and 300 km to the north. The domains were large enough in consideration of the scale of the synoptic event while avoiding influences of the domain boundaries. The extents of the domains were also selected to be inclusive of the Mississippi and Ohio Rivers, a section of the Great Lakes, the Appalachian Region, and parts of the Atlantic.

Figure 2.1. The inner and outer domains with respect to the contiguous US and Kentucky counties.

The model was initialized for a single event of August 3, 2001 (Figure 2.2) at 0300Z and for a period of 40 hours. This ensured that the main precipitation event would

be captured. This includes the initial synoptic event and the subsequent mesoscale events. The WRF model was initialized with NCEP's NARR data with a horizontal resolution of 32 km (Mesinger et al., 2006). This dataset was created with NCEP's regional Eta model and assimilation system and Noah LSM. The NARR dataset was created at three-hour intervals. Therefore, there were a total of 13 updates during the simulation. The initial seven hours were used as spin-up time for the model, with the following 24-hour period to include a full diurnal cycle.

Figure 2.2. The observations and synoptic conditions on the day of interest (HPC/CPC, 2001).

2.2. Land Cover Changes

As part of the research, there were 20 experiments performed based on variations of land cover and topography on known surface mine locations in eastern Kentucky (Figure 2.3). The initial simulations were the control of current land cover (post-2001). Subsequently, surface mined areas were altered to bare soil, grass, and forest. Additional simulations were then performed by increasing the area of the altered land cover by 5, 10, 15, and 30% respectively. These were completed to determine the sensitivity of the model to LCC. Then the final set of simulations involved increased topography for both control and LCC simulations to approximate pre-MTR conditions.

Specifically, the analysis was focused on five areas in eastern Kentucky. These areas were selected due to surface mine concentrations. These areas are designated as A through E with each area a size of 0.3° x 0.3 ° (878 km^2), roughly the average county size of Kentucky (872.0 km^2). Moreover, land cover for each area of interest was primarily of deciduous broadleaf forests (Figure 2.3). For example, area A had the smallest percentage of deciduous forest (84%).

Each land cover had its own set of biophysical properties, such as albedo, roughness length, root depth, and stomotal resistance (Table 2.1). Albedo pertains to the ability to reflect radiation. Roughness length is the height where structures interfere with local wind flow, causing turbulence, and stomatal resistance refers to a plant's ability to transpire under certain conditions.

Figure 2.3. Eastern Kentucky Land Cover with known Surface Mines as of 2002 with selected areas for analysis.

Table 2.1. Various biophysical properties of land-cover categories.

Land Cover	Albedo	Roughness Length (m)	Maximum Root Depth (cm)	Stomatal Resistance (s^{-1})
Deciduous Forest	0.16	0.50	200	100
Mixed Forest	0.13	0.50	200	125
Cropland/Grassland	0.18	0.14	100	40
Cropland/Woodland	0.16	0.20	100	70
Savanna	0.20	0.15	100	70

The locations for LCC simulations were selected from Kentucky statewide mined areas as of 2002. These were developed by the Kentucky Geological Survey (KGN, 2002). Note that, with respect to surface mining, there was no representative USGS dataset available for WRF. However, from the previously mentioned KGN (2002) data, there were 1892 separate locations for surface mining found (Figure 2.3). After isolating eastern Kentucky surface mines, the individual features were merged and the feature class was then transformed into a raster. The mined area cells were then given a value of one, while all other cells were assigned a value of zero. The raster was then converted to an ASCII file and then into binary with an associated index file. The binary was then read into WRF Preprocessing System (WPS) using the index file, the geogrid table, and the process domain module.

2.3. GIS Applications

With respect to altered area coverage, the mines were also buffered in a GIS. This was done until each feature reached the minimum thresholds of 5, 10, 15, and 30% of the original area respectively. Then the feature classes were prepared as before in order to be read into the WRF model via WPS. With respect to elevation alteration, the first step was to determine the center of each of the mine features. The distance from

each centroid to the mined area edge was then determined, along with the maximum distance, in raster format. Then a ratio of the actual distance to the maximum distance was calculated and subtracted from one; this resulted in a gradient where the centroid had a value of one decreasing toward the edges of the mine area (Figure 2.4). The non-defined areas were reclassified to zero prior to the raster conversion to ASCII and subsequently to binary. After reading the data into WPS, the elevation was increased by a multiplicative factor of 152.4m (500ft) to represent pre-MTR elevations.

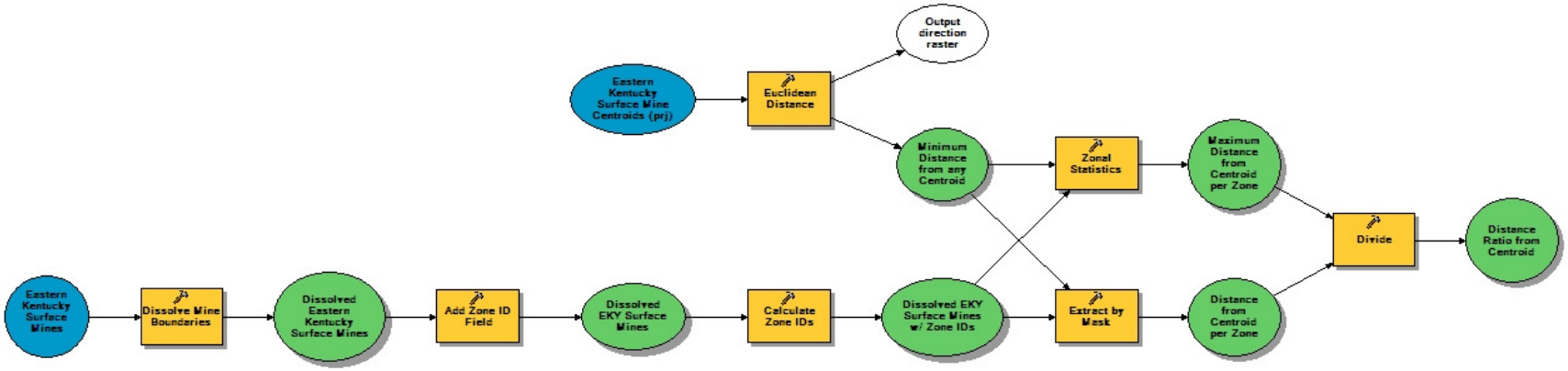

Figure 2.4. Flow Chart with the progression of tools in ESRI's ArcGIS Model Builder for creating gradients per surface mine feature based on distance from the center of a given feature and the maximum distance.

Chapter 3

Results

The following discussion includes results from the control and sensitivity experiments. Each section begins with the summary highlights followed by the results from area A through E. The summary remarks for each set of experiments are at the end of each section.

3.1. Control Simulation for Areas A-E: Precipitation, latent (*LE*) and sensible heat flux (*H*), planetary boundary layer height (*PBLH*), and equivalent potential temperature (θ_e)

The timing of initial precipitation for the five regions varied from 1300 Z to 1600 Z with maximum precipitation occurred anywhere from 1400 Z to 2000 Z (Figure 3.1). Average precipitation for all five area was 22.38 mm for the 24-hour period while totals for individual area ranged from 9.00 mm (area E) to 36.34 mm (area B).Overall, average *LE* and *H* for all five areas were 70 and 19 W m^{-2}, respectively. The hourly *LE* for the 24 hr. simulation period ranged from -9 to 370 W m^{-2}, while the *H* was from -23 to 176 W m^{-2}. By location, the lowest average *LE* for the 24-hour period was 60 W m^{-2} at area B, while the highest value was 93 W m^{-2} at area E. With respect to *H*, the minimum average value was at area C with 13 W m^{-2}, while the maximum was at area E with 32 Wm^{-2} (Table 3.1; Appendix: Tables 1-5).

Area A reached its peak hourly precipitation (6.56 mm) at 2000 Z, while both the *H* and *LE* peaked at 1500 Z at 150 and 240 W m^{-2}, respectively (Figure 3.1a;

Appendix: Table 1). At the time of the heaviest precipitation, the strongest part of the storm was in the northern sector. This resulted in strong updrafts and downdrafts throughout the county-sized region, allowing θ_e advection (as seen by perpendicular wind barbs and the contours of θ_e) primarily involving a slightly drier air mass, represented by the lower θ_e values, from 900 to 600 hPa (Figure 3.2). Also, along with the updrafts, the planetary boundary layer height (*PBLH*) was higher (400 m) than the area impacted by the downdrafts. Precipitation amounts in the downdraft regions reached 25 to 50 mm with localized amounts greater than 50 mm. Due to these conditions, the *H* was suppressed to less than 100 W m^{-2}, while the *LE* was surpassed 200 W m^{-2} in some locations.

Table 3.1. Fluxes and precipitation for all five areas over 24 hours. These include the increased elevation simulation (pre-MTR) and simulations based on increased area for the respective land-cover.

Composite (min-max)	***H* (Wm^{-2})**	***LE* (Wm^{-2})**	**Total Precipitation (mm)**
Control	18.96 (-23.00-176.32)	69.84 (-9.13-370.28)	22.38 (9.00-36.34)
pre-MTR	18.50 (-22.14-152.31)	71.65 (-8.76-329.08)	24.21 (12.50-39.63)
Bare Soil	24.62 (-21.03-152.22)	50.25 (-8.36-234.30)	11.39 (5.67-17.95)
5%	23.96 (-21.08-154.10)	49.88 (-8.36-218.74)	14.22 (5.50-28.07)
10%	20.75 (-20.94-151.58)	46.30 (-8.45-241.28)	14.86 (6.17-24.58)
15%	21.08 (-21.47-144.87)	47.75 (-8.40-229.57)	16.32 (9.69-23.71)
30%	22.32 (-20.97-155.98)	48.39 (-8.41-254.32)	15.58 (7.97-24.19)
pre-MTR	18.42 (-20.87-135.48)	44.50 (-8.32-214.66)	17.36 (4.79-37.16)
Grass	16.90 (-22.86-153.99)	73.16 (-9.10-344.53)	23.17 (7.45-34.81)
5%	18.33 (-22.85-148.57)	75.65 (-9.46-314.72)	18.71 (10.98-30.12)
10%	16.68 (-22.42-147.09)	74.02 (-9.08-329.86)	18.96 (10.97-27.79)
15%	17.53 (-22.54-165.54)	72.05 (-9.33-369.55)	18.96 (5.87-35.56)
30%	15.80 (-23.35-144.89)	70.63 (-9.10-308.09)	22.40 (11.00-34.42)
pre-MTR	16.75 (-21.69-149.44)	70.39 (-9.42-333.84)	20.17 (7.20-33.07)
Forest	18.07 (-22.87-163.32)	69.77 (-8.99-349.44)	22.78 (12.33-38.18)
5%	20.00 (-23.21-157.43)	73.55 (-8.60-302.79)	20.18 (11.72-28.94)
10%	20.00 (-23.21-157.43)	73.55 (-8.60-302.79)	20.18 (11.72-28.94)
15%	18.44 (-23.13-157.24)	70.47 (-8.57-364.52)	22.51 (11.08-39.60)
30%	20.60 (-23.47-172.89)	73.19 (-8.53-327.15)	19.47 (12.05-28.83)
pre-MTR	19.57 (-22.13-158.49)	73.06 (-9.61-329.85)	19.60 (7.39-30.53)

Area B reached to its peak hourly precipitation (10.35 mm) at the same time as area A. However, the peaks in the *LE* and *H* did not coincide. The peak *H* (88 W m^{-2}) was reached at 1300 Z but the *LE* peaked at 1800 Z with a value of 268 W m^{-2} (Figure 3.1b; Appendix: Table 2). Also, area B had weaker thunderstorms than area A. The strongest updrafts were along the western and southern edges of the region, and strong downdrafts were in the center of area B as well as along the eastern edge (Figure 3.3). With the strong vertical winds there was θ_e advection from just below 900 hPa to 600 hPa, though the *PBLH* were less than 200 m for most of the area. Heavier precipitation amounts correlate with the strong downdrafts, with the localized totals exceeding 75 mm. Similar to area A, *H* was low for area B, however the *LE* had less coverage, exceeding 200 W m^{-2} with the higher quantities to the north and west.

Area C reached its peak hourly precipitation (4.26 mm) at 1700 Z, following the peak in the *H* (93 W m^{-2}) at 1400 Z and preceding the highest *LE* (233W m^{-2}) at 1900 Z (Figure 3.1c; Appendix: Table 3). At the time of the peak in precipitation over the central and the north-eastern sections, PBL exceeded 400 m with localized areas exceeding 600 m where strong updrafts were present (Figure 3.4). These updrafts along with strong downdrafts resulted in vertical extension of θ_e, allowing for the replacement of a layer of dry air from 950 to 600 hPa that developed due to precipitation. However, even with the introduction of more moist air the precipitation amounts remain 25 mm or less, except in the eastern edge where *H* reached 200 W m^{-2} and the *LE* reached up to 500 W m^{-2}.

Figure 3.1. Hourly (GMT) fluxes and precipitation for the control simulation for (a) Area A, (b) Area B, (c) Area C, (d) Area D, and (e) Area E.

Figure 3.2. Control simulation for Area A at 20z with (a) DBZ, (b) PBLH (m), (c) vertical winds (cms^{-1}) at 825mb, (d) total precipitation (mm), (e) sensible heat flux (Wm^{-2}), (f) latent heat flux (Wm^{-2}), (g) vertical theta-e cross-section on 37.11˚ N, and (h) vertical theta-e cross-section on 83.12˚ W.

Figure 3.3. Control simulation for Area B at 20z (a) DBZ, (b) PBLH (m), (c) vertical winds (cm s^{-1}) at 825mb, (d) total precipitation (mm), (e) sensible heat flux (Wm^{-2}), (f) latent heat flux (Wm^{-2}), (g) vertical theta-e cross-section on 37.326˚ N, and (h) vertical theta-e cross-section on 82.89˚ W.

Figure 3.4. Control simulation for Area C at 17z with (a) DBZ, (b) PBLH (m), (c) vertical winds (cm s^{-1}) at 825mb, (d) total precipitation (mm), (e) sensible heat flux (Wm^{-2}), (f) latent heat flux (Wm^{-2}), (g) vertical theta-e cross-section on 37.31˚ N, and (h) vertical theta-e cross-section on 82.77˚ W.

Area D experienced maximum precipitation of 8.19 mm at 1400 Z, while *H* and *LE* peaked at 102 and 311 W m^{-2}, respectively, at 1700 Z. The peak in the fluxes coincided with a break in the precipitation (Figure 3.1d; Appendix: Table 4). With multiple thunderstorms, there were multiple pockets of both updraft and downdrafts. This allowed for θ_e extension from 400 down to 800 hPa and from the surface up to 800 hPa (Figure 3.5). Also, associated with the training of the thunderstorms, were two areas with precipitation exceeding 25 mm, at one location precipitation reached 75 mm. The *PBLH*, at this time and location, was associated with strong updrafts, areas yet to be impacted by thunderstorms, and areas of higher *H* and *LE*. Due to the breaks in the thunderstorms in the east, the *H* was able to reach 200 W m^{-2}, while the *LE* up to 300 W m^{-2}.

Area E reached its peak precipitation at 1700 Z (area average of 3.64 mm) (Figure 3.1e; Appendix: Table 4), with isolated locations exceeding 25 mm. There were associated vertical winds θ_e advection from 500 hPa to 700 hPa and from the surface to 700 hPa, in particular there was a break in a layer of drier air due to a thunderstorm downdraft (Figure 3.6). The limited extent of the thunderstorms allowed the *H* to reach 300 W m^{-2}, in the northern corners of the site, while the *LE* exceeded 500 W m^{-2} in isolated locations. It was in these areas of higher *H* and *LE* that *PBLH* was the highest, reaching up to 800 m. However, the peaks in the *H* and *LE* were not reached until 1900 Z, the area averages being 176 and 370 W m^{-2} respectively (Figure 3.6; Appendix: Table 4).

Figure 3.5. Control simulation for Area D at 14z with (a) DBZ, (b) PBLH (m), (c) vertical winds (cm s^{-1}) at 825mb, (d) total precipitation (mm), (e) sensible heat flux (Wm^{-2}), (f) latent heat flux (Wm^{-2}), (g) vertical theta-e cross-section on 37.62˚ N, and (h) vertical theta-e cross-section on 82.695˚ W.

Figure 3.6. Control simulation for Area E at 17z with (a) DBZ, (b) PBLH (m), (c) vertical winds (cm s^{-1}) at 825mb, (d) total precipitation (mm), (e) sensible heat flux (Wm^{-2}), (f) latent heat flux (Wm^{-2}), (g) vertical theta-e cross-section on 37.495° N, and (h) vertical theta-e cross-section on 82.275° W.

Overall, both *H* and *LE* were high for the control simulation when supported by updrafts allowing for a more stable *PBL* reaching up to 176 Wm^{-2} and 370 Wm^{-2} respectively, thus allowing for more atmospheric moisture for precipitation. In this simulation, precipitation varied by location ranging from 9 to 36 mm with hourly rates of 4 to 10 mm (Table 3.1; Appendix: Tables 1-5; Figure 3.1). The next simulation to be considered is the forest land cover simulation.

3.2. Forest Simulation: Precipitation, *LE*, *H*, *PBLH*, and θ_e

For forest experiments, precipitation started between 1300 Z to 1600 Z for the five areas (A-E). Subsequently, precipitation peaked between 1400 Z to 1900 Z (Figure 3.7). While the average precipitation for five areas was 22.78 mm for the 24-hour period, the total precipitation for these areas ranged from 12.33 mm (area E) to 38.18 mm (area A). The average precipitation was only 0.4 mm higher than the control simulation, though the minimum precipitation was higher by 3.33 mm and the maximum higher by only 1.84 mm. Also, the maximum precipitation was estimated for area B instead of A for the forest simulation (Table 3.1; Appendix: Tables 1-5).

Average *LE* and *H* for these five areas were 70 and 18 W m^{-2}, respectively. Both are within 1 W m^{-2} of the control values. The *LE* ranged from -9 to 349 W m^{-2}, while the *H* was from -23 to 163 W m^{-2}. The minimum *LE* was within 1 W m^{-2} of the control, while the maximum was less than the control simulation by almost 21 W m^{-2}. With respect to the *H*, the minimum value was about the same as control and the maximum was 13 W m^{-2} less than control. By location, the lowest average *LE* for the 24-hour period was 59 W m^{-2} at area D (control value was 60 W m^{-2} at area B), with the highest value of 89 W m^{-2} at area E. The latter was 3 W m^{-2} lower than the control (at area E).

The minimum average value for *H* was 11 W m^{-2} at area D while previously it was 13 W m^{-2} at area C. Moreover, the maximum was 27 W m^{-2} at area E while it was 32 W m^{-2} at the same area (Table 3.1; Appendix: Tables 1-5).

Figure 3.7. Refer to Figure 3.1 but with respect to the Forest Land-Cover Simulation.

Area A reached to its peak hourly precipitation rate an hour earlier than the control (at 1900 Z), though the area average value is similar to that of control (10.32

mm). However, the timing of the peak *H* (163 W m^{-2}) and *LE* (245 W $m^{-2)}$ shifted to 1500 Z (Figure 3.7a; Appendix: Table 1). In this simulation, at 2000 Z, the strongest part of the storm was located in the northern sector of location A. It was located slightly south compared to the control simulation and less intense, resulting in strong updrafts and downdrafts throughout the county-sized region (Figure 3.8). Accompanied with the downdrafts were precipitation amounts reaching 50 to 75 mm, which was 25 mm greater than the precipitation estimated by control simulation. Despite these changes, the *H* was still suppressed to less than 100 W m^{-2}. In contrast, *LE* surpassed 200 Wm^{-2} in some locations, though in a lesser extent than control. With respect to θ_e, there were higher values at 700 and 600 hPa. These higher values were in close proximity to strong down drafts and precipitation. The higher *PBLH*, however, had less coverage than in the control simulation and coincide with higher *H* and/or strong updrafts.

Area B reached to its peak hourly precipitation (area average of 7.97 mm) at 1600 Z, which was four hours earlier than the control (Figure 3.7b; Appendix: Table 2). The strongest updrafts were scattered across the southern half of the region with strong downdrafts mainly to the northern third (Figure 3.9). Due to the lack of thunderstorm development, shown in the decreased vertical motion, the precipitation in area B was significantly lower with only localized areas exceeding 50 mm. At area B, *H* exceeded 100 W m^{-2} and *LE* 300 W m^{-2}. Associated with the higher *H* and *LE,* were higher *PBLH*. With respect to θ_e , the lower part of the troposphere has lower values except for close to the surface, which was coinciding with downdrafts and precipitation.

Figure 3.8. Refer to Figure 3.2 with respect to the Forest Simulation.

Figure 3.9. Refer to Figure 3.3 with respect to the Forest Simulation.

Area C reached to its peak hourly precipitation at 1700 Z, the same time as the control. However, the area average value increased from the control to 7.64 mm and the *H* (100 W m^{-2}) and the *LE* (287 W m^{-2}) both peaked at 1900 Z (Figure 3.7c; Appendix: Table 3). Strong vertical winds were more prominent in the south and east (Figure 3.10). With the change in the distribution of the vertical winds, the areal extent of precipitation was also altered and two additional areas where amounts exceeding 25 mm were found. As expected, there was also a redistribution of the *H* with a few areas that only reached 200 W m^{-2}, while the *LE* reached up to 400 W m^{-2} instead of the previous 500 W m^{-2}. Associated with these fluxes was high *PBLH* and could be found in the western part of area C. At the surface θ_e values were higher than control, with drier air extending from 850 hPa to 600 hPa and linked to an end of precipitation.

At area D, the precipitation peaked at 1400 Z (area average of 7.84 mm) (Figure 3.7d; Appendix: Table 4). With multiple thunderstorms, vertical circulation was extended up to 500 hPa, a weak circulation at 700 hPa and an associated divergence at the surface (Figure 3.11). This circulation interfered with the advection of θ_e in com-parison to the control simulation due to subsidence. Associated with the training of thunderstorms were two areas with precipitation exceeding 25 mm and, in one location, up to 75 mm. Due to the breaks in the thunderstorms in the East, the *H* was able to reach 200 W m^{-2}, while the *LE* reached up to 300 W m^{-2}. Due to widespread storms, in contrast to the control, the higher values of the *LE* and *H* were more constrained, as were the associated *PBLH*. The fluxes in this simulation did not peak for another two hours after control, with an area average of 245 W m^{-2} for *LE* and 72 W m^{-2} for *H* heat fluxes. They were lower than control by 66 and 30 W m^{-2}, respectively (Figure 3.7d; Appendix: Table 4).

Figure 3.10. Refer to Figure 3.4 with respect to the Forest Simulation.

Figure 3.11. Refer to Figure 3.5 with respect to the Forest Simulation.

Area E had less developed thunderstorms and they were located more to the west than the control. Also, the peak precipitation occurred an hour earlier than the control at 1600 Z (Figure 3.7e). By 1700 Z, the precipitation distribution, both temporally and spatially, was generally similar to the control except that there were two locations reaching 50 mm (Figure 3.12). General trend of the fluxes and precipitation during the simulation were similar to the control, excluding the spike in precipitation at 1600 Z in the control (Figure 3.7e). There were associated vertical winds that extended to 500 hPa, very similar to the control simulation. Vertical profile of θ_e is generally similar in both simulations (Figure 3.12). *H* and *LE* were 300 and 500 W m^{-2}, with isolated locations along the eastern edge exceeding the latter value. Area average precipitation, *H*, and *LE* were 5.43 mm, 153 W m^{-2}, and 349 W m^{-2}, respectively (Appendix: Table 4). Despite these similarities, control simulation had a higher area average flux for both *LE* and *H*, had lower area average precipitation, and higher values of *PBLH* over a larger area.

Figure 3.12. Refer to Figure 3.6 with respect to the Forest Simulation.

Overall, both *H* and *LE* were slightly lower for the forest simulation than control, supported by updrafts allowing for a more stable *PBL* reaching up to 163 Wm^{-2} and 349 Wm^{-2} respectively, allowing for atmospheric moisture for precipitation. In this simulation, the area average precipitation varied by location ranging from 12 to 38 mm with hourly rates of 5 to 10 mm, both similar to that of control (Table 3.1; Appendix: Tables 1-5; Figure 3.7). The next simulation to be considered is the grass land cover simulation.

3.3 Grass Simulation: Precipitation, *LE*, *H*, *PBLH*, and θ_e

The precipitation for the five regions began between 1300 Z to 1600 Z with maximum between 1600 Z to 2000 Z (Figure 3.13). The average total from area A-E was 23.17 mm for the 24-hour period. Total precipitation ranged from 7.45 mm (area E) to 34.81 mm (area A). Average *LE* and *H* for five area were 73 and 17 W m^{-2}, respectively. By location, the lowest average *LE* for the 24-hour period was 62 W m^{-2} (area D) with the highest value was 94 W m^{-2} (area E). With respect to *H* the minimum average value was 12 W m^{-2} (area D) while the maximum was 27 W m^{-2} (area E) (Table 3.1; Appendix: Tables 1-5).

Area A reached to its peak hourly precipitation at 1900 Z, which was an hour earlier than control simulation. The average precipitation was 7.91 mm. As in the control simulation, precipitation occurred several hours after sunrise allowing for early peaks in both *H* (154 W m^{-2}) and *LE* (290 W m^{-2}) at 1500 Z (Figure 3.13a; Appendix: Table 1). By 2000 Z, the surrounding conditions were distinctly different from the control. The most intense thunderstorm shift from the north in the control to the northwest instead. Furthermore, there were multiple thunderstorm cells in the south that were not present in

the control (Figure 3.14). There were also presence of strong updrafts but was restricted to the west and northwest away from the center of site. The presence of strong downdrafts was more pronounced in the central and southern sections of area A (Figure 3.14). The *PBLH* values were higher in vicinity of the strong updrafts and the areas of higher *H*. In comparison to the control, the *PBLH* was higher most likely due to the updrafts and higher *H*. θ_e advection occurred due to the vertical winds. However, there was a drier air mass from 800 to 600 hPa coinciding with strong downdrafts. Compared to control, θ_e was higher at the surface, coinciding with presence of more precipitation. Also, in area A grass simulation, the drier air mass capped the moist air of the surface. Accompanied with the downdrafts, higher precipitation amounts were more prevalent over larger area compared to control simulation. It was found that the precipitation reached 25 to 50 mm for two bands, while the band associated with the downdraft near the center of area A was reaching up to 75 mm (Figure 3.14). Due to these conditions, the *H* was suppressed to less than 100 W m^{-2} with exception to a small area in the northwest, while the *LE* surpassed 200 W m^{-2} in several locations (Figure 3.14).

Area B reached to its peak hourly precipitation at the same time as for control and also maintained the somewhat similar general trends of the hourly fluxes and precipitation, like the control simulation. The area average precipitation reached 9.95 mm while the *H* and *LE* peaked two hours earlier at 106 and 325 W m^{-2}, respectively (Figure 3.13b; Appendix: Table 2). The storms in the area were centered in the area of interest instead of being in the south and east. There were fewer strong updrafts with the strongest in the southwestern corner with strong downdrafts being in the central part of the area and along the northeastern corner (Figure 3.15). With the lack of strong updrafts

there was little θ_e advection near 900 hPa. Also, due to downdrafts and limited *H*, the *PBLH* lowered to less than 400 m with higher values more prominent in the southeast in comparison to the control, reaching heights up to 600 m. For control simulation *PBLH* was higher over the northeast. Additionally, there was a small change in precipitation with amounts reaching up to 75 mm, while the control simulation reached up to 101 mm in two different locations in area B. However, like the control simulation, while *LE* was exceeding 200 W m^{-2}, the higher values were to the southeast instead of the northwest.

Figure 3.13. Refer to Figure 3.1 but with respect to the Grass Land-Cover Simulation.

Figure 3.14. Refer to Figure 3.2 with respect to the Grass Simulation.

Figure 3.15. Refer to Figure 3.3 with respect to the Grass Simulation.

Area C reached to its peak hourly precipitation rate at 1700 Z. Hourly distribution of precipitation and fluxes maintained similar pattern like control simulation. Area average precipitation for area C was 4.47 mm and the area average fluxes peaked at 88 W m^{-2} and 280 W m^{-2} for *H* and *LE* respectively (Figure 3.13c; Appendix: Table 3). The thunderstorm in the east was similar to that of the control; however, storms, as identified by localized maxima of dbz and associated vertical winds, in the west moved to the south (Figure 3.16). Though there were still strong vertical winds present, they were mainly updrafts and the few resulting downdrafts were only able to provide precipitation amounts of 25 mm or less with exception to the northeastern edge (Figure 3.16). The downdrafts also impacted the θ_e profile. The drier air, represented by the lower θ_e values, extended down to the surface and similar to control. Also, there was influence of updrafts on the θ_e profile as the layer of drier air remained intact (Figure 3.16). The updrafts, when coinciding with high *H*, allowed for the development of the *PBL*, with heights reaching 600 m. In this region, there were small areas where *H* reached up to 200 W m^{-2}, while the *LE* up to 400 W m^{-2} instead of 500 W m^{-2} of control (Figure 3.16).

The precipitation peaked at 1900 Z for area D and area average precipitation was 5.58 mm. Area average *H* (80 W m^{-2}) and the *LE* (249 W m^{-2}) peaked two hours earlier (Figure 3.13d; Appendix: Table 4). There were several strong updrafts in the area similar to the control (Figure 3.17). These impacted the θ_e profile along more warm/moist air to 700 hPa, while downdafts allowed upper level θ_e to advect down to 700 hPa resulting in the decomposition of the drier air mass existing from 800 to 600 hPa similar to the control. The updrafts along with the *H* coincide with the higher values of *PBLH*, but not as high as the control, only reaching 600 m. However there were strong downdrafts

resulting in two small areas with precipitation ranging between 25-50 mm. Due to the breaks in the thunderstorms in the east, the *H* reached 200 W m^{-2}, while the *LE* up to 300 W m^{-2}.

Area E reached to its peak precipitation rates at 1600 Z, an hour earlier than the control. Area average precipitation was 3.17 mm (Figure 3.13e; Appendix: Table 4). Local total precipitation at 1700 Z exceeded 25 mm for only one location (Figure 3.18). The updrafts associated with the storms resulted in advection of θ_e into the 800 and 700 hPa from the surface, similar to the control simulation. Due the isolated nature of these thunderstorms, *H* reached to 300 W m^{-2} in more locations than the control and the *LE* to 500 W m^{-2} also over most of the areas. Along with the higher *H*, there were higher *PBLH* with greater areal extent reaching 1000 m.

Figure 3.16. Refer to Figure 3.4 with respect to the Grass Simulation.

Figure 3.17. Refer to Figure 3.5 with respect to the Grass Simulation.

Figure 3.18. Refer to Figure 3.6 with respect to the Grass Simulation.

Overall, both *H* and *LE* were, slightly lower for the grass simulation than either forest or control, supported by updrafts allowing for a more stable *PBL* reaching up to 154 Wm^{-2} and 345 Wm^{-2} respectively (Table 3.1; Appendix: Tables 1-5), allowing for atmospheric moisture for precipitation. In this simulation, area average precipitation varied by location ranging from 7 to 35 mm with hourly rates of 3 to 10 mm, both slightly less than that of the forest or control simulations (Figure 3.13). The next simulation to be considered is the bare soil land cover simulation.

3.4. Bare Soil Simulation: Precipitation, *LE*, *H*, *PBLH*, and θ_e

The beginning of initial precipitation for the five regions varied from 1300 Z to 1600 Z with peaks anywhere from 1500 Z to 1900 Z (Figure 3.19). While the precipitation averaged at 23.17 mm for a 24-hour period, the total precipitation among various area ranged from 7.45 mm (area E) to 34.81 mm (area A). Overall, the average *LE* and *H* were 50 and 25 W m^{-2}. The *LE* ranged from -8 to 234 W m^{-2}, while the *H* from -21 to 154 W m^{-2}. By location, the lowest area average *LE* for the 24-hour period was 42 W m^{-2} (area B) with the highest value was 65 W m^{-2} (area E). With respect to *H*, the minimum area average value was at area D with 18 W m^{-2}, while the maximum was at area E with 31 W m^{-2} (Table 3.1; Appendix: Tables 1-5).

Area A reached its peak hourly precipitation (7.68 mm) at 1900 Z which was one hour earlier compared to that of the control. The peak fluxes, however, coincided with the control run at 1500 Z with 154 W m^{-2} for *H* and 169 W m^{-2} for *LE* (Figure 3.19a; Appendix: Table 1). At 2000 Z, there were areas of strong updrafts and downdrafts but most of the area A was under the influence of weak downdrafts (Figure 3.20). Accompanied with the downdrafts was precipitation reaching 25 to 50 mm. The weak

downdrafts and updrafts allowed for limited advection of θ_e leaving a mostly undisturbed layer of relatively dry air from 850 to 600 hPa, in contrast to control. Under these conditions, the *H* was able to exceed 100 W m^{-2} in the northwestern corner, while the *LE* surpassed 300 W m^{-2} in some locations. Coinciding with both relatively high *LE* and *H* were higher values of *PBLH*, which also coincided with two areas of relatively strong updrafts.

Figure 3.19. Refer to Figure 3.1 but with respect to the Bare Soil Land-Cover Simulation.

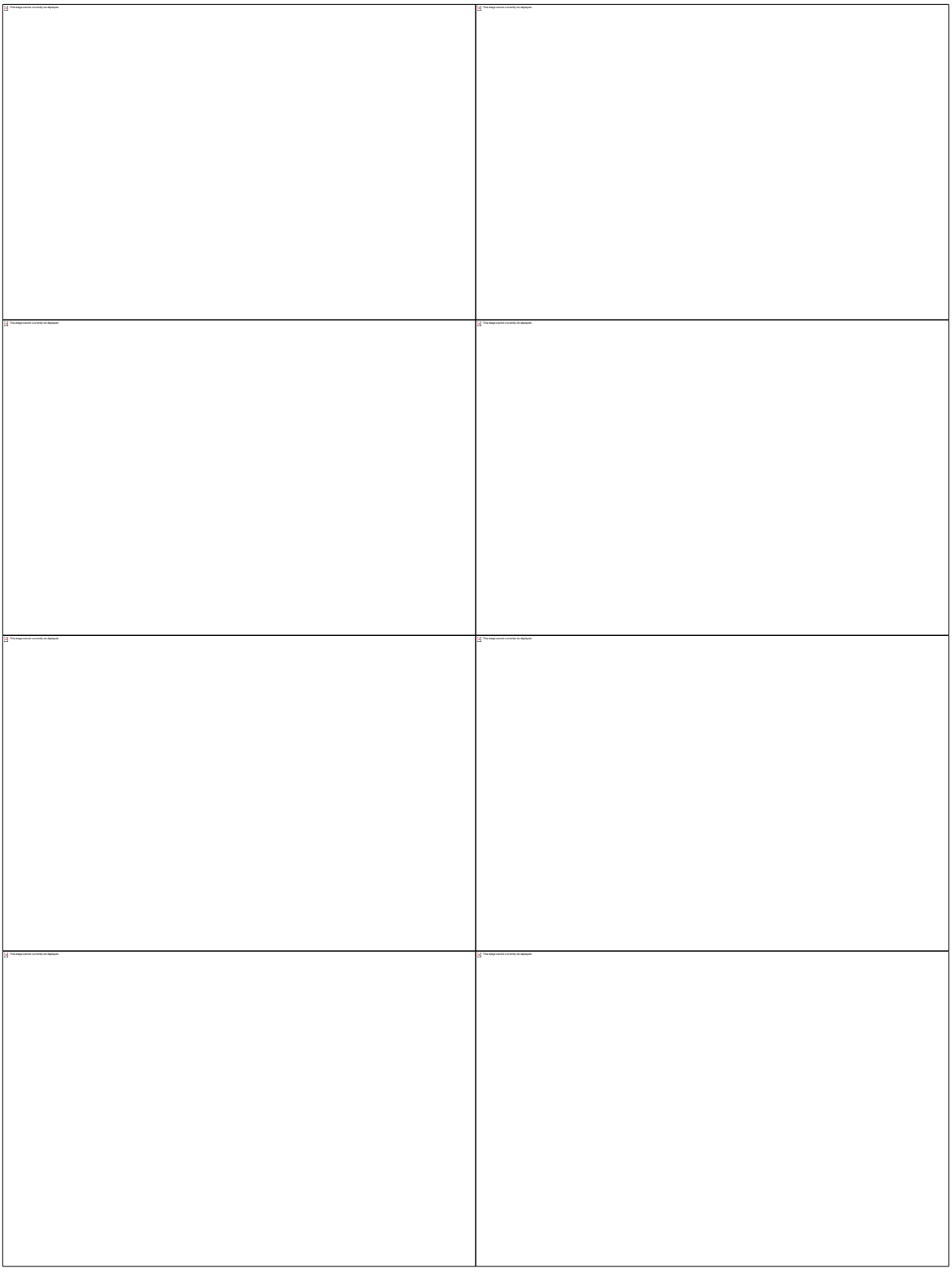

Figure 3.20. Refer to Figure 3.2 with respect to the Bare Soil Simulation.

Area B reached its peak hourly precipitation (5.98 mm) at 1600 Z. *H* peaked two hours later than the control simulation at 104 W m^{-2}, while the *LE* peaked at 1800 Z with only 143 W m^{-2} (Figure 3.19b; Appendix: Table 2). There was only one location with updraft, which was in the southwestern corner, while there were two separate downdrafts (Figure 3.21). One occupies the same location like the control simulation; however, the second downdraft was located where a strong updraft previously existed. In the θ_e cross-section, there was not enough vertical motion to promote θ_e advection, in contrast to the control where there was advection as well as a large air mass of relatively dry air. With respect to precipitation, there were only two locations where it exceeds 25 mm compared to the control where precipitation amounts were exceeding 50 mm with isolated amounts exceeding 75 mm. This area had a few locations where *H* reached 100 W m^{-2} while the *LE* exceeding 200 W m^{-2} (Figure 3.21). Coinciding with this was the *PBLH* up to 800 m, in contrast to the control simulation with 400 m.

Area C reached its peak hourly precipitation at 1700 Z, the same as control. Area average precipitation was 6.04 mm. The peak *LE* and *H* were 154 and 113 W m^{-2}, respectively. They occurred at 1900 and 2000 Z (Figure 3.19c; Appendix: Table 3). The thunderstorm in the east was similar to that of the control; however, the location of western storms of this area moved further to the east (Figure 3.22). Though there were still strong vertical winds present, they were mainly updrafts and precipitation was 25 mm or less with exception to the northeastern edge. With respect to the θ_e, the stronger updrafts were conducive of advection from 900 to 800 hPa but not enough to penetrate the layer of dry air as it was achieved in the control simulation. In this region, *H* was up to 200 W m^{-2}, while the *LE* 300 W m^{-2}. The latter is much lower than the control's 500 W

m^{-2}. *PBLH* of 800 m coincided with higher velocity updrafts, higher *H* and *LE*, similar to that of the control simulation.

At area D, precipitation reached its peak of 3.63 mm at 1500 Z which is hour later than control simulation. The peak area average *LE* (187 W m^{-2}) occurred at 1700 Z, as in the control simulation, while the area average *H* peaked (101 W m-2) at 1900 Z (Figure 3.19d; Appendix: Table 4). The updrafts resulted in the advection of θ_e into a layer of drier air (Figure 3.23). With the weaker storms than the control, the precipitation (25 mm) was limited to only over an isolated location and a large area with no precipitation. Due to the breaks in the thunderstorms in the east and the limited precipitation, the *H* and *LE* were able to reach 200 W m^{-2}. It was in areas of higher *H* and updrafts that the *PBLH* was able to develop up to 600 m, instead of the control's 800 m.

Area E in this simulation reached its peak area average precipitation, *H* and *LE* an hour before than the control run. Area average precipitation maximum was 2.22 mm, which occurred at 1600 Z. Peak area average *H* and *LE* were 152 and 234 W m^{-2}, respectively (Figure 3.19e; Appendix: Table 4). For the bare soil simulation, there was only one main cell instead of multiple cells found in the control (Figure 3.24). The updrafts from this cell allowed for θ_e advection found in the vertical column of the θ_e profile with higher value than the drier air at 900 to 500 hPa. Due to the lack of thunderstorm development, precipitation was largely limited to 25 mm or less. For the same reason, *H* reached up to 300 W m^{-2} to the north and east and *LE* to 500 W m^{-2}. The higher values of both types of fluxes as well as the occurrence of updrafts prompted the development of the *PBL* with heights up to 1000 m.

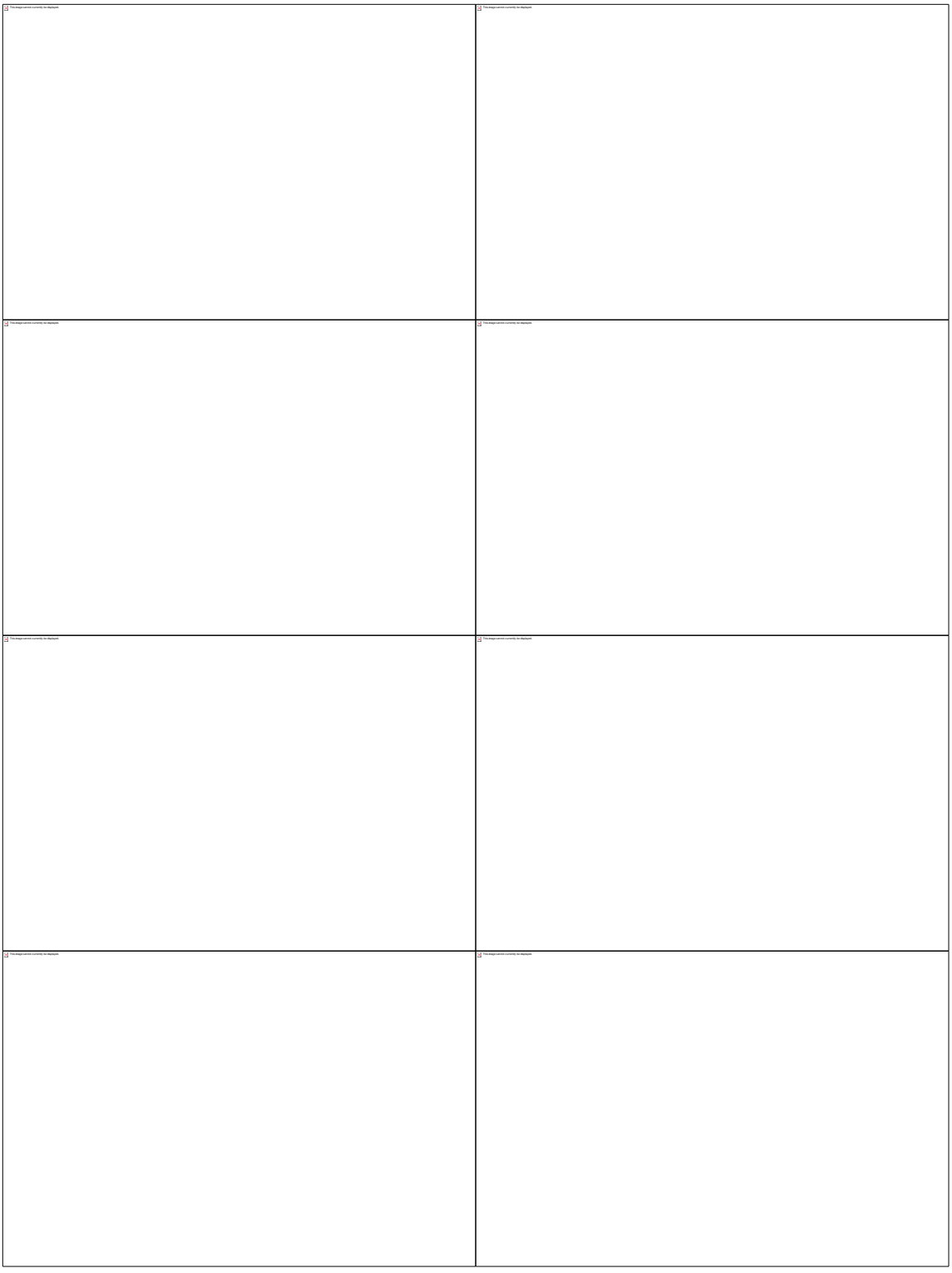

Figure 3.21. Refer to Figure 3.3 with respect to the Bare Soil Simulation.

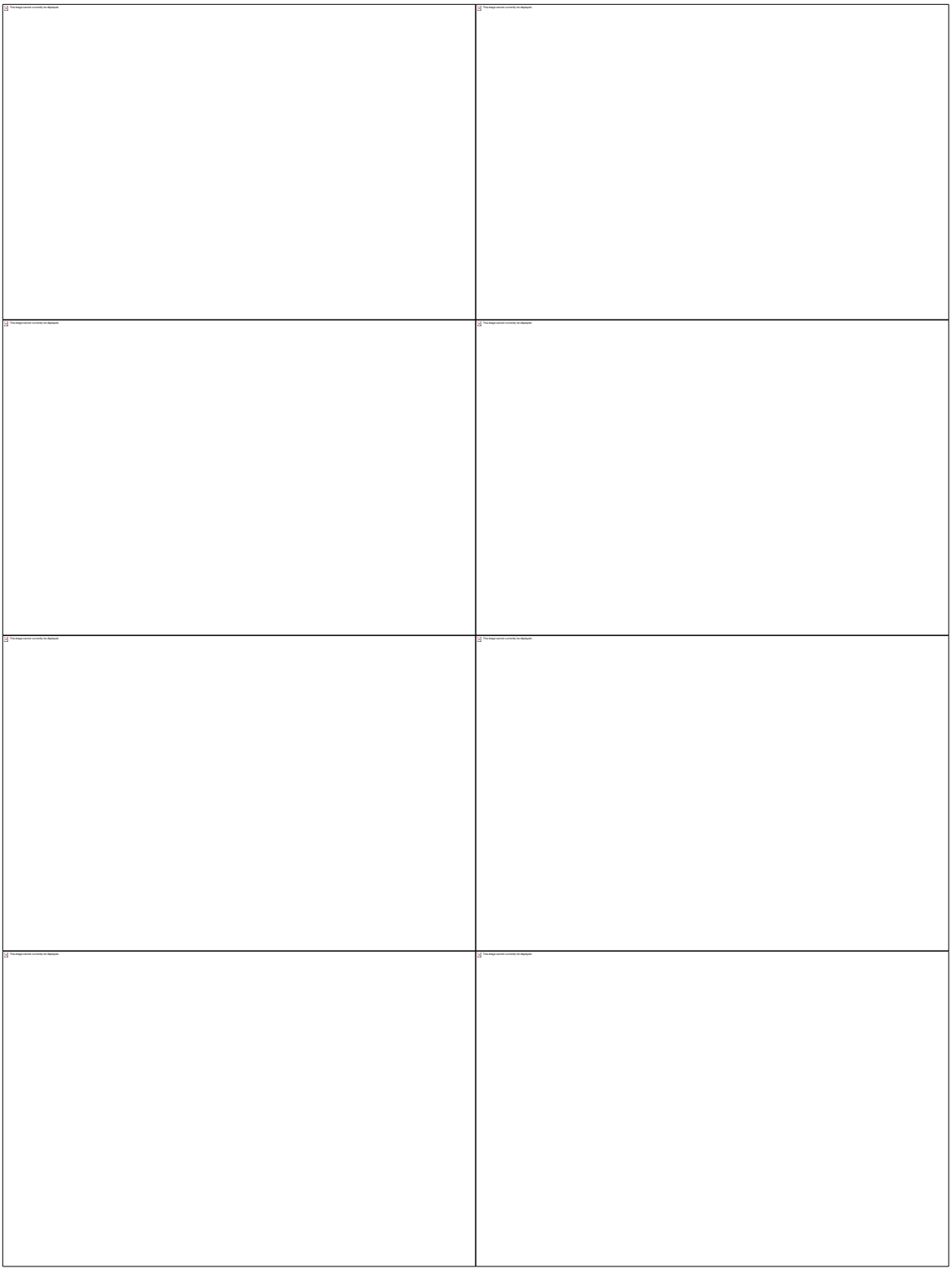

Figure 3.22. Refer to Figure 3.4 with respect to the Bare Soil Simulation.

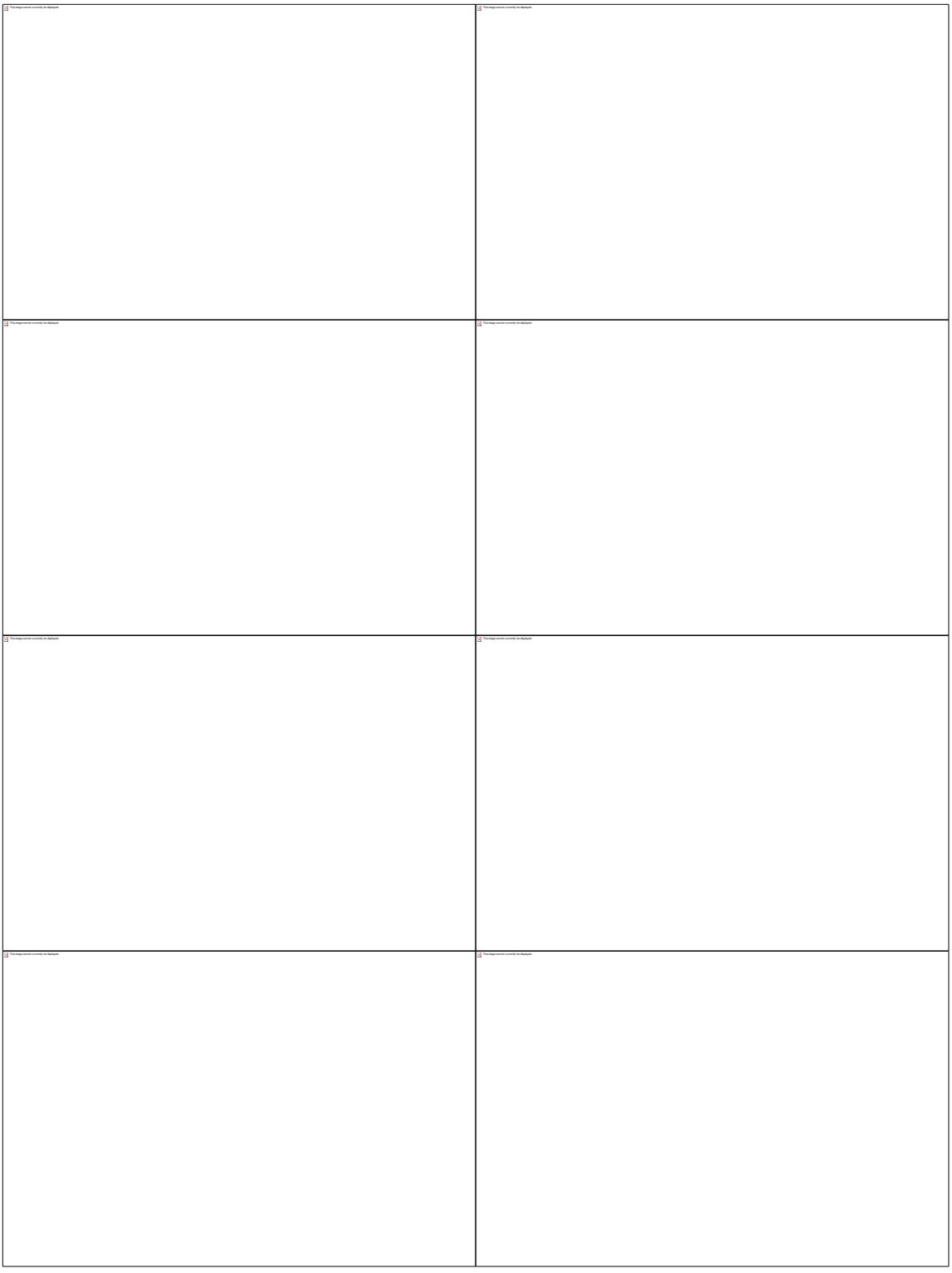

Figure 3.23. Refer to Figure 3.5 with respect to the Bare Soil Simulation.

Figure 3.24. Refer to Figure 3.6 with respect to the Bare Soil Simulation.

Overall, in contrast to previously mentioned simulations, *H* only reached up to 154 Wm^{-2} but with a higher mean of 27 Wm^{-2} in comparison to control's 20 Wm^{-2} over 24-hours and *LE* reaching only 234 Wm^{-2} for area averages (Table 3.1; Appendix: Tables 1-5). The fluxes are higher in isolated locations along with higher PBLH accompanied by updrafts, compared to surrounding areas, allowing for atmospheric moisture for precipitation however limited. In this simulation, area average precipitation varied by location ranging from 6 to 18 mm with hourly rates of 2 to 6 mm, significantly less than previous simulations (Table 3.1; Appendix: Tables 1-5; Figure 3.19). The next simulation to be considered is the increased elevation simulation.

3.5. Increased Elevation Simulation: Precipitation, *LE*, *H*, *PBLH*, and θ_e

The timing of the beginning of precipitation for the five locations varied from 1300 Z to 1600 Z, with peak precipitation occurred sometime between 1500 to 1900 Z (Figure 3.25). While the average precipitation for all areas was 24 mm for the 24-hour simulation period, the total precipitation ranged from 12.50 mm (area E) to 39.63 mm (area A). Overall, average *LE* and *H* were 72 and 19 W m^{-2}, respectively. The *LE* ranged from -9 to 329 W m^{-2}, while the *H* from -22 to 152 W m^{-2}. By location, the lowest average *LE* for the 24-hour period was 64 W m^{-2} (area D) and the highest was 88 W m^{-2} (area E). For *H* the minimum average was 14 W m^{-2} (area B) while the maximum was 27 W m^{-2} (area E) (Table 3.1; Appendix: Tables 1-5).

Area A reached its peak hourly precipitation at 1700 Z, instead of 2000 Z in the control simulation, with an area average of 8.69 mm. While the timing of the peak precipitation differs from control, the timing of the peaks of the *H* (152 W m^{-2}) and *LE* (232 W m^{-2}) were the same as control (1500 Z) (Figure 3.25a; Appendix: Table 1). At

2000 Z, instead of one intense storm to the north in the control simulation, there were three relatively less intense storms to the northwest, west, and southwest (Figure 3.26). Along with multiple thunderstorms, there were more regions of strong updrafts and downdrafts. Accompanied these storms was precipitation, reaching 25 to 50 mm with a considerable area receiving amounts from 50 to 75 mm. Associated with the downdrafts linked to these storms was cooler and drier air as seen in the θ_e cross-section (Figure 3.26), while the updrafts brought warmer moister air. Due to breaks in the storm activity at 2000 Z, the *H* surpassed 100 W m^{-2} in a few locations, while the *LE* exceeded 300 W m^{-2} in some locations, particularly in the area of highest precipitation. The *PBLH* was coincided primarily with higher *H,* reaching 800 m, surpassing the control simulation by 400 m (Figure 3.26).

At 1600 Z, Area B reached its peak area average precipitation of 6.79 mm with the fluxes following the general trend of the control run. *H* reached 86 W m^{-2} and the *LE* at 233 W m^{-2} (Figure 3.25b; Appendix: Table 2). The activity at 2000 Z was pre-dominately along the edges of area B with strongest storms to the south, southwest, west, and northwest (Figure 3.27). There were several areas of strong updrafts while there was a broad region of strong downdrafts adjacent to the updrafts. Though the downdrafts were associated with precipitation, the heavier amounts were associated with a combination of training and downdrafts resulting in localized totals exceeding 50 mm. The downdrafts were associated with cooler and dryer air and thus resulted in lower θ_e. With the breaks in the thunderstorms, *H* was able to surpass 100 W m^{-2}. However the *LE*, due to moisture availability, also exceeded 300 W m^{-2}. The *PBLH,* partly in response to the updrafts and the *H* and *LE*, reached up to 800 m, exceeding the control.

Area C reached its peak hourly precipitation at 1700 Z with an area average of 8.08 mm with the *H* and *LE* reaching a high at 1800 Z with 99 and 291 W m^{-2} respectively (Figure 3.25c; Appendix: Table 3). At 1700 Z, there were strong thunderstorms in the southeastern corner (Figure 3.28). With these thunderstorms there were strong updrafts and downdrafts allowing for heavier amounts of precipitation from 25 to 75 mm. The updrafts, while impacting the θ_e, were not able to penetrate the drier air aloft from 850 to 600 hPa. In this site, there were small areas in the northeast and southwest where *H* reached 200 W m^{-2} due to breaks in thunderstorm activity, while the *LE* up to 500 Wm^{-2}. *PBLH* corresponds to the *H* and updrafts reaching 800 m similar to control.

Area D, during this simulation, unlike the control run, experienced its peak rainfall at 1500 Z reaching 7.42 mm (Figure 3.25d; Appendix: Table 4). At 1400 Z, there were multiple strong thunderstorms cells, though not as intense as in the control (Figure 3.29). However, there were strong vertical motions and precipitation ranged from 25 to 50 mm. These vertical winds impacted both θ_e and *PBLH*. With respect to θ_e there was advection in the upper troposphere down to 600 hPa. The downdrafts in the lower troposphere resulted in advection of lower θ_e associated with cooler and drier air. The updrafts, however, moved warmer and moister air raising θ_e values and higher *PBLH*. The *PBLH*, with influence of *H* and updrafts, reached 600 m which was 200 m less than the control. Though there were breaks in the thunderstorms in the east of this site, the *H* was suppressed below 100 W m^{-2} and the *LE* was limited to 200 W m^{-2}. Both area average *LE* and *H* peaked later in the simulation at 1800 Z and 1900 Z at 329 and 127 W m^{-2}, respectively.

Figure 3.25. Refer to Figure 3.1 with respect to the Increased Elevation Simulation.

Figure 3.26. Refer to Figure 3.2 with respect to the Increased Elevation Simulation.

Figure 3.27. Refer to Figure 3.3 with respect to the Increased Elevation Simulation.

Figure 3.28. Refer to Figure 3.4 with respect to the Increased Elevation Simulation.

Figure 3.29. Refer to Figure 3.5 with respect to the Increased Elevation Simulation.

Figure 3.30. Refer to Figure 3.6 with respect to the Increased Elevation Simulation.

Area E reached its peak precipitation at 1600 Z, an hour earlier than the control simulation. Area average precipitation was 4.45 mm (Figure 3.25e; Appendix: Table 4), however, totals ranged between 25 to 50 mm. At 1700 Z, the thunderstorms were more scattered which allowed the *H* to reach 300 W m^{-2} to the north and the *LE* to reach 500 W m^{-2} with isolated locations exceeding 500 W m^{-2} (Figure 3.30). At 1700 Z, there were several updrafts and downdrafts associated with various storms. The downdrafts were contributors to the precipitation and therefore the atmospheric moisture content and thus impacting θ_e. The updrafts resulted in advection of warm, moist air and thus higher values of θ_e. The updrafts along with the *H* and possibly *LE* contributed to the *PBLH*, reaching 1000 m.

Overall, both *H* and *LE* were slightly lower than control or forest, though H was similar to the grass simulation, supported by updrafts allowing for a more stable *PBL* reaching up to 163 Wm^{-2} and 349 Wm^{-2} respectively (Table 3.1; Appendix: Tables 1-5), allowing for atmospheric moisture for precipitation. In this simulation, area average precipitation varied by location ranging from 13 to 40 mm with hourly rates of 4 to 9 mm, both similar to that of control and forest (Table 3.1; Appendix: Tables 1-5; Figure 3.25).

3.6. Summary

In short, LCC impacted several meteorological parameters including *H*, *LE*, and precipitation. The control simulation reported that *H* and *LE* were reaching up to 176 and 370 Wm^{-2}, respectively. For bare soil, they reached up to 154 and 234 Wm^{-2} (Table 3.1). Subsequently, changing the LC to grass resulted in *H* being similar to bare soil with maxima at 154 Wm^{-2}. *LE* was significantly higher than bare soil but comparable to both

forest and control, peaking at 345 Wm^{-2} (Table 3.1). For the forest simulation, both *H* and *LE* were slightly lower reaching up to 163 and 349 Wm^{-2}. However, they were higher than grass simulation. Then with the increased elevation simulation, both *H* and *LE* were slightly lower than control and equaled to forest at 163 and 349 Wm^{-2}.

The changes in LC altered other parameters. There were changes in the wind fields and this resulted in changes in *PBLH* as well as moisture transport leading to changes in θ_e. These changes were reflected in precipitation. In the control simulation, precipitation varied by area (A-E) and ranged from 9 to 36 mm with hourly rates of 4 to 10 mm (Table 3.1; Figure 3.1). With the changes in LC to bare soil, area average precipitation varied from 6 to 18 mm for different areas (A-E) with hourly rates of 2 to 6 mm, significantly less than previous simulations (Table 3.1; Figure 3.19). Precipitation for the grass simulation, however, ranged from 7 to 35 mm for the area averages, with hourly rates of 3 to 10 mm. This was an increase from bare soil but slightly less than that of the control simulation (Table 3.1; Figure 3.13). In the forest simulation, the area average precipitation ranged from 12 to 38 mm with hourly rates of 5 to 10 mm, both similar to that of control (Table 3.1; Figure 3.7). Then in the increased elevation simulation, the area average precipitation, ranged from 13 to 40 mm for different areas (A-E) with hourly rates of 4 to 9 mm, both similar to that of control and forest (Table 3.1; Figure 3.25).

Chapter 4

Conclusions

The objective of this research was to understand the impacts of MTR-related LCC on a flash flood-producing heavy rainfall event in Eastern Kentucky. For this purpose, we have conducted a mesoscale model sensitivity study using the WRF model. The implementation of WRF involved the use of the original LC as well as modified LC. These modifications include changing MTR areas to bare soil, grass, and forest. The impacts of topography were also considered.

During the course of this research, the sensitivities of atmospheric responses to LCC and the elevation were investigated. It was established that both LCC and changes in the elevation at the MTR locations resulted in changes to the surface energy and moisture budget, the PBL, and the wind fields. For example, area B with bare soil experienced the largest changes (24 mm less) in precipitation, compared to the control simulation. The same area also experienced the largest changes in *LE* (-157 Wm^{-2}). Compared to control, the largest difference in *H* was 73 Wm^{-2} for area E (Table 3.1; Appendix: Tables 1-5). We suspect that the initial changes to the meteorological conditions were due to the changes in the vegetation types (e. g., grass vs. forest) which also resulted in modification of albedo, LAI, stomatal regulation, canopy height, and root distribution. Compared to forest, grass has a lower stomata resistance and higher LAI (Appendix: Table 6), counteracting the impact of lower root depth on the evapotranspiration. Also, since the control LC was largely forest, the difference between control and forest simulation was quite similar while bare soil simulations produced the most notable differences on. Again, these were primarily due to the larger

albedo, lower roughness length, and limited moisture availability. In addition, these changes were linked to lack of vegetation and limited water holding capacity of bare soil, which limited latent energy fluxes. Moreover, the bare soil simulation had a higher albedo impacting net radiation.

Overall, the control simulation produced the higher values in fluxes as well as precipitation. With respect to *H* and *LE*, the control simulation produced the highest values of 176 and 370 W m^{-2}, respectively, while bare soil simulations produced the lowest values of 135 and 215 W m^{-2}. Precipitation, however, was the highest (40 mm) for the increased elevation, while bare soil simulation produced the lowest (6 mm) (Table 3.1). Forest and control simulations were more similar to each other where fluxes and precipitation showed minimal difference. The grass simulations produced a larger range for *H* (16-18 W m^{-2}) and *LE* (73-76 W m^{-2}), while producing lower precipitation ranges (18-23 mm) compared to control (Table 3.1).

For this study a number of simulations were completed addressing changes in topography and LCC representing MTR. The forest with increased elevation was represented as a potential pre-MTR simulation. The post-MTR sites were represented by the bare soil simulation, followed by the grass and forest simulations with progressive vegetative growth. With this progression, there was an initial decrease in precipitation, which was recovered after the growth of grasslands due to the access to subsurface water and higher rates of evapotranspiration.

In short, LCC impacts the boundary layer altering daytime mixing, convection and cloud cover. These variables affected the drag and impacting horizontal wind speeds resulting in vertical winds due to differences in the velocity through the vertical column

and the subsequent turbulence of the boundary layer. This led to changes in moisture convergence and energy fluxes and further impacting both temperature and precipitation.

As indicated above, the primary focus of this research was precipitation. The area-average 24-hr precipitation ranged from 13 to 40 mm in the pre-MTR scenario for the five study areas (A to E). With the conversion of LC from MTR, there was a noticeable decrease in precipitation ranged from 6 to 18 mm for the five areas. Subsequently, with the growth of grassland, the precipitation increase ranged from 7 to 35 mm. Then, continuing the progression of LCC with respect to forest, the precipitation ranged from 12 mm to 38 mm for the five areas (Table 3.1).

This model-sensitivity study has found that that LCC and, in particular, MTR has impacted the flash flood-producing rain event. However, this does not cover the full impacts of LCC on the local hydrology. With bare soil (post-MTR), there could be less precipitation but a higher probability of runoff due to lack of vegetation. Also, there is a need to investigate the impacts of downwind precipitation from the LCC.

In addition, we recommend for the use of higher resolution land cover data and model simulations to properly represent land-cover and elevation changes. Application of remote sensing would be useful for accurately capturing current land cover including surface mines (Townsend et al., 2009). Current model resolution of elevation data is 30 seconds, though higher resolution data could be developed through the integration of digital elevation models (DEMs) leading to potential research involving updating WRF reference geographic dataset.

REFERENCES

Adegoke, J. O., Pielke Sr, R., and Carleton, A. M. (2007). Observational and modeling studies of the impacts of agriculture-related land use change on planetary boundary layer processes in the central US. *Agricultural and Forest Meteorology*, *142*(2), 203-215.

Chen, S. H., and Dudhia, J. (2000). Annual report: WRF physics. *Air Force Weather Agency*. Online at: http://www2.mmm.ucar.edu/wrf/users/docs/wrf-doc-physics.pdf.

Clough, S. A., Shephard, M. W., Mlawer, E. J., Delamere, J. S., Iacono, M. J., Cady-Pereira, K., Boukabara, S., and Brown, P. D. (2005). Atmospheric radiative transfer modeling: A summary of the AER codes. *Journal of Quantitative Spectroscopy and Radiative Transfer*, *91*(2), 233-244.

Demchak, J., Skousen, J., and McDonald, L. M. (2004). Longevity of acid discharges from underground mines located above the regional water table. *Journal of Environmental Quality*, *33*(2), 656-668.

Eastman, J. L., Coughenour, M. B., and Pielke Sr, R. A. (2001). Does grazing affect regional climate? *Journal of Hydrometeorology*, *2*(3), 243-253.

Fox, J. (1999). Mountaintop Removal in West Virginia An Environmental Sacrifice Zone. *Organization & Environment*, *12*(2), 163-183.

Gero, A. F., Pitman, A. J., Narisma, G. T., Jacobson, C., and Pielke, R. A. (2006). The impact of land cover change on storms in the Sydney Basin, Australia. *Global and Planetary Change*, *54*(1), 57-78.

Hartman, K. J., Kaller, M. D., Howell, J. W., and Sweka, J. A. (2005). How much do valley fills influence headwater streams?. *Hydrobiologia*, *532*(1-3), 91-102.

Holl, K. D. (2002). Long-term vegetation recovery on reclaimed coal surface mines in the eastern USA. *Journal of Applied Ecology*, *39*(6), 960-970.

Hong, S. Y., and Lim, J. O. J. (2006). The WRF single-moment 6-class microphysics scheme (WSM6). *Journal of the Korean Meteorological Society, 42*(2), 129-151.

HPC/CPC (Hydrological Prediction Center and Climate Prediction Center) (2001). Daily Weather Maps Weekly Series July 30 – August 5, 2001. Available fromhttp://docs.lib.noaa.gov/ rescue/dwm/data_rescue_daily_weather_maps.html. Accessed 2013.

Hu, X.M., Nielsen-Gammon, J.W., and Zhang, F. (2010). Evaluation of three planetary boundary layer schemes in the WRF model. *Journal of Applied Meteorology and Climatology*, 49(9), 1831-1844.

Kain, J.S. (2004). The Kain-Fritsch convective parameterization: an update. *Journal of Applied Meteorology*, 43(1), 170-181.

KGN (Kentucky Geography Network and Kentucky Geological Survey) (2002). Statewide Mined Out Areas (FGDC) / Statewide Mined Out Areas (ISO). Available from http://kygisserver.ky.gov/geoportal/catalog/search/resource/details.page?uuid={98DA4C1F-9026-4FCC-96D3-2B76585CDC69}. Accessed 2013.

Loveland, T. R. and Acevedo, W. (2012) Land Cover Change in the Eastern United States. Available from http://landcovertrends.usgs.gov/east/regionalSummary.html. Accessed 2013.

Matthews, H. D., Weaver, A. J., Eby, M., and Meissner, K. J. (2003). Radiative forcing of climate by historical land cover change. *Geophysical Research Letters*, *30*(2), 1055.

Mesinger, F., DiMego, G., Kalnay, E., Mitchell, K., Shafran, P. C., Ebisuzaki, W., JOVIć, D., Woollen, J., Rogers, E., Berbery, E. H., Ek, M. B., Fan, Y., Grumbine, R., Higgins, W., Li, H., Lin, Y., Manikin, G., Parrish, D., and Shi, W. (2006). North American regional reanalysis. *Bulletin of the American Meteorological Society*, *87*(3), 343-360.

Narisma, G. T., and Pitman, A. J. (2003). The impact of 200 years of land cover change on the Australian near-surface climate. *Journal of Hydrometeorology*, *4*(2), 424-436.

Pan, H. L., and Mahrt, L. (1987). Interaction between soil hydrology and boundary-layer development. *Boundary-Layer Meteorology*, *38*(1-2), 185-202.

Phillips, J. D. (2004). Impacts of surface mine valley fills on headwater floods in eastern Kentucky. *Environmental Geology*, *45*(3), 367-380.

Pielke, R. A., Adegoke, J., Beltran-Przekurat, A., Hiemstra, C. A., Lin, J., Nair, U. S., Niyogi, D., and Nobis, T. E. (2007). An overview of regional land-use and land-cover impacts on rainfall. *Tellus B*, *59*(3), 587-601.

Pitman, A. J., Narisma, G. T., Pielke, R. A., and Holbrook, N. J. (2004). Impact of land cover change on the climate of southwest Western Australia. *Journal of Geophysical Research: Atmospheres (1984–2012)*, *109*(D18), 1-.1028/2003JD004347.

Oke, T. R. (1987). Boundary Layer Climates. 2nd Edn. London: Methuen

Sayler, K. L. (2012a). Central Appalachians. Available from http://landcovertrends.usgs.gov/east/eco69Report.html. Accessed 2013.

Sayler, K. L. (2012b). Western Allegheny Plateau. Available from http://landcovertrends.usgs.gov/east/eco70Report.html. Accessed 2013.

Schneider, N., and Eugster, W. (2005). Historical land use changes and mesoscale summer climate on the Swiss Plateau. *Journal of Geophysical Research: Atmospheres (1984–2012)*, *110*(D19), 10.1029/2004JD005215.

Simmons, J. A., Currie, W. S., Eshleman, K. N., Kuers, K., Monteleone, S., Negley, T. L., Pohlad, R., and Thomas, C. L. (2008). Forest to reclaimed mine land use change leads to altered ecosystem structure and function. *Ecological Applications*, *18*(1), 104-118.

Siqueira, M., Katul, G., and Porporato, A. (2009). Soil moisture feedbacks on convection triggers: the role of soil-plant hydrodynamics. *Journal of Hydrometeorology*, *10*(1), 96-112.

Skousen, J., Cook, T., Wilson-Kokos, L., and Pena-Yewtukhiw, E. (2013) Survival and growth of Chestnut backcross seeds and seedlings on surface mines. *Journal of Environmental Quality*, 42(3), 690-695.

Sohl, T. L. (2012). Southwestern Appalachians. Available from http://landcovertrends.usgs.gov/east/eco68Report.html. Accessed 2013.

Sridhar, V., Elliott, R. L., Chen, F., and Brotzge, J. A. (2002). Validation of the NOAH-OSU land surface model using surface flux measurements in Oklahoma. *Journal of Geophysical Research: Atmospheres (1984–2012)*, *107*(D20), ACL-3.

Tanny, J., Cohen, S., Assouline, S., Lange, F., Grava, A., Berger, D., Teltch, B., and Parlange, M. B. (2008). Evaporation from a small water reservoir: Direct measurements and estimates. *Journal of Hydrology*, 351(1–2), 218-229.

Townsend, P. A., Helmers, D. P., Kingdon, C. C.McNeil, B. E., de Beurs, K. M., and Eshleman, K. N. (2009). Changes in the extent of surface mining and reclamation in the Central Appalachians detected using a 1976–2006 Landsat time series, Remote Sensing of Environment, 113(1), 62-72.

Velde, R., Su, Z., Ek, M., Rodell, M., and Ma, Y. (2009). Influence of thermodynamic soil and vegetation parameterizations on the simulation of soil temperature states and surface fluxes by the Noah LSM over a Tibetan plateau site. *Hydrology and Earth System Sciences*, *13*(6), 759-777.

Wang, W., Bruyère, C., Duda, M., Dudhia, J., Gill, D., Lin, H.C., Michalakes, J., Rizvi, S., and Zhang, X. (2010). WRF-ARW Version 3 Modeling System User's Guide. Boulder, CO: Mesoscale & Microscale Meteorology Division, National Center for Atmospheric Research,

APPENDIX

Table 1. Fluxes and precipitation for Area A over 24 hours. This was done for control, bare soil, grass, and forest simulations. Also, this includes the increased elevation simulation (pre-MTR) and simulations based off increased area for the respective land-cover.

Area A		*H* (Wm^{-2})	*LE* (Wm^{-2})	Total Precipitation (mm)
Control		19.91 (-22.34-150.19)	65.17 (-9.13-240.18)	26.51
	pre-MTR	20.11 (-22.03-152.31)	69.84 (-8.76-232.33)	39.63
Bare Soil		27.15 (-19.98-154.22)	52.09 (-8.36-168.53)	17.95
	5%	22.53 (-20.33-154.10)	48.83 (-8.36-167.74)	28.07
	10%	25.75 (-20.21-132.76)	47.63 (-8.45-181.03)	24.58
	15%	25.31 (-20.03-144.55)	48.65 (-8.40-192.74)	16.60
	30%	24.39 (-20.20-141.27)	48.73 (-8.41-207.50)	22.10
	pre-MTR	24.14 (-20.04-125.79)	47.78 (-8.32-167.05)	10.35
Grass		17.56 (-21.70-153.99)	67.28 (-9.10-289.79)	34.81
	5%	19.74 (-21.75-148.57)	72.58 (-9.04-280.16)	30.12
	10%	16.95 (-21.80-147.09)	69.55 (-9.08-274.71)	25.34
	15%	15.29 (-21.85-150.91)	62.92 (-9.13-283.63)	35.56
	30%	16.13 (-21.77-144.89)	63.43 (-9.10-274.10)	28.11
	pre-MTR	19.72 (-21.65-149.44)	66.36 (-9.42-276.31)	18.98
Forest		19.40 (-22.26-163.32)	63.08 (-8.56-245.15)	38.18
	5%	22.70 (-22.21-157.43)	74.22 (-8.60-269.51)	20.14
	10%	22.70 (-22.21-157.43)	74.22 (-8.60-269.51)	20.14
	15%	22.35 (-22.52-167.24)	71.71 (-8.57-249.63)	26.00
	30%	23.78 (-22.50-172.89)	70.48 (-8.53-263.87)	22.84
	pre-MTR	22.35 (-21.75-158.49)	70.67 (-9.61-281.72)	19.48

Table 2. Average value across for Area B over 24 hours. This was done for control, bare soil, grass, and forest simulations. Also, this includes the increased elevation simulation (pre-MTR) and simulations based off increased area for the respective land-cover.

Area B		*H* (Wm^{-2})	*LE* (Wm^{-2})	Total Precipitation (mm)
Control		13.06 (-23.00-88.10)	60.19 (-8.07-268.43)	36.34
	pre-MTR	14.22 (-21.20-85.99)	65.50 (-6.72-233.23)	22.35
Bare Soil		23.46 (-19.59-104.13)	42.19 (-3.22-143.07)	12.32
	5%	19.98 (-19.35-100.98)	39.79 (-6.57-165.61)	16.93
	10%	16.14 (-19.48-90.24)	35.80 (-4.86-111.00)	16.12
	15%	15.45 (-19.51-75.13)	36.02 (-5.83-122.54)	21.58
	30%	17.09 (-19.20-98.70)	38.50 (-3.77-176.62)	24.19
	pre-MTR	9.51 (-19.01-67.90)	31.01 (-7.08-108.28)	37.16
Grass		15.45 (-22.09-105.58)	68.27 (-904-324.58)	32.21
	5%	16.65 (-21.24-96.51)	69.91 (-9.46-273.90)	19.98
	10%	12.74 (-21.81-76.41)	66.64 (-6.35-239.16)	27.79
	15%	11.60 (-22.14-73.44)	59.03 (-9.33-185.19)	25.92
	30%	12.25 (-21.81-86.40)	62.11 (-8.45-250.38)	34.42
	pre-MTR	14.43 (-20.85-85.89)	67.07 (-8.70-272.42)	33.07
Forest		16.97 (-22.87-116.30)	68.04 (-8.99-310.21)	21.89
	5%	17.19 (-23.21-104.20)	70.62 (-7.52-281.21)	28.94
	10%	17.19 (-23.21-104.20)	70.62 (-7.52-281.21)	28.94
	15%	18.51 (-22.69-98.35)	68.27 (-8.22-226.55)	17.83
	30%	21.89 (-22.86-120.93)	78.33 (-8.06-327.15)	21.11
	pre-MTR	13.61 (-22.13-93.95)	64.68 (-8.99-256.63)	30.53

Table 3. Average value across for Area C, over 24 hours. This was done for control, bare soil, grass, and forest simulations. Also, this includes the increased elevation simulation (pre-MTR) and simulations based off increased area for the respective land-cover.

Area C		*H* (Wm^{-2})	*LE* (Wm^{-2})	Total Precipitation (mm)
Control		12.72 (-23.00-93.37)	64.94 (-7.30-233.24)	13.99
	pre-MTR	14.77 (-22.14-98.63)	70.55 (-3.33-291.26)	16.51
Bare Soil		24.05 (-21.03-112.62)	44.84 (-2.74-154.49)	9.71
	5%	26.41 (-21.08-138.47)	43.83 (-2.68-168.39)	5.94
	10%	17.43 (-20.94-85.00)	36.42 (-5.02-129.54)	6.17
	15%	21.43 (-21.47-116.10)	44.19 (-3.10-162.53)	10.03
	30%	19.84 (-20.97-84.78)	38.68 (-3.77-127.85)	8.11
	pre-MTR	18.00 (-20.87-87.59)	38.40 (-4.39-127.01)	8.10
Grass		12.54 (-22.86-87.82)	73.80 (-6.41-279.70)	14.37
	5%	16.71 (-22.85-72.25)	77.67 (-6.81-227.81)	10.98
	10%	12.55 (-22.42-75.37)	71.87 (-5.48-230.52)	11.39
	15%	14.89 (-22.54-90.91)	74.32 (-7.43-301.21)	8.78
	30%	14.00 (-23.35-81.37)	74.34 (-6.92-276.11)	12.75
	pre-MTR	11.49 (-21.69-74.54)	65.08 (-9.17-253.68)	17.37
Forest		15.67 (-22.85-99.62)	69.89 (-5.52-287.44)	16.81
	5%	16.95 (-23.07-94.52)	68.44 (-4.69-228.93)	19.05
	10%	16.95 (-23.07-94.52)	68.44 (-4.69-228.93)	19.05
	15%	11.43 (-23.13-92.78)	64.32 (-4.02-204.28)	18.02
	30%	17.88 (-23.47-107.53)	70.25 (-6.61-251.36)	12.54
	pre-MTR	15.24 (-22.06-87.87)	70.66 (-5.62-278.31)	17.80

Table 4. Average value across for Area D over 24 hours. This was done for control, bare soil, grass, and forest simulations. Also, this includes the increased elevation simulation (pre-MTR) and simulations based off increased area for the respective land-cover.

Area D		*H* (Wm^{-2})	*LE* (Wm^{-2})	Total Precipitation (mm)
Control		17.46 (-17.61-101.82)	66.08 (-6.86-310.74)	26.06
	pre-MTR	16.01 (-18.21-127.02)	64.29 (-5.03-329.08)	30.04
Bare Soil		17.66 (-16.85-101.18)	47.03 (-4.81-184.86)	11.32
	5%	19.65 (-17.04-108.67)	51.17 (-1.48-197.13)	14.65
	10%	13.77 (-16.80-73.62)	44.57 (-3.92-168.81)	18.67
	15%	14.08 (-17.31-92.18)	44.87 (-3.42-201.85)	23.71
	30%	16.49 (-16.85-117.60)	47.09 (-3.00-215.55)	15.52
	pre-MTR	11.57 (-17.81-83.49)	43.15 (-4.62-170.13)	26.37
Grass		12.03 (-17.65-79.81)	62.39 (-6.12-249.24)	27.01
	5%	13.96 (-17.71-104.44)	66.50 (-5.61-314.72)	18.67
	10%	16.38 (-17.24-112.80)	69.56 (-4.44-321.18)	19.29
	15%	13.85 (-17.44-71.09)	65.26 (-6.92-242.75)	18.66
	30%	12.32 (-17.96-84.08)	63.76 (-4.92-257.25)	25.71
	pre-MTR	12.50 (-17.60-76.91)	60.65 (-7.23-224.37)	24.23
Forest		10.89 (-17.67-72.13)	58.78 (-5.30-245.35)	24.72
	5%	15.65 (-17.95-130.07)	63.20 (-4.07-283.41)	21.04
	10%	15.65 (-17.95-130.07)	63.20 (-4.07-283.41)	21.04
	15%	10.51 (-18.05-56.71)	59.20 (-4.32-203.28)	39.60
	30%	11.06 (-17.78-66.97)	56.84 (-6.92-217.58)	28.83
	pre-MTR	13.83 (-18.28-106.91)	64.28 (-5.94-303.86)	22.79

Table 5. Average value across for Area E over 24 hours. This was done for control, bare soil, grass, and forest simulations. Also, this includes the increased elevation simulation (pre-MTR) and simulations based off increased area for the respective land-cover.

Area E		*H* (Wm^{-2})	*LE* (Wm^{-2})	Total Precipitation (mm)
Control		31.66 (-17.87-176.32)	92.80 (-7.01-370.28)	9.00
	pre-MTR	27.37 (-18.45-131.13)	88.03 (-5.57-325.44)	12.50
Bare Soil		30.77 (-16.30-151.57)	65.08 (-4.18-234.30)	5.67
	5%	31.26 (-16.39-150.76)	65.78 (-3.02-218.74)	5.50
	10%	30.69 (-16.16-151.58)	67.09 (-3.14-241.28)	8.77
	15%	29.15 (-16.34-144.87)	65.00 (-3.30-229.57)	9.69
	30%	33.80 (-16.17-155.98)	68.97 (-1.19-254.32)	7.97
	pre-MTR	28.88 (-17.02-135.48)	62.17 (-2.50-214.66)	4.79
Grass		26.94 (-17.40-130.99)	94.07 (-5.42-344.53)	7.45
	5%	24.59 (-17.45-103.02)	91.59 (-6.92-298.75)	13.81
	10%	24.78 (-17.42-116.67)	92.47 (-4.74-329.86)	10.97
	15%	32.01 (-17.55-165.64)	98.75 (-7.73-369.55)	5.87
	30%	24.29 (-17.47-114.91)	89.50 (-5.81-308.09)	11.00
	pre-MTR	25.61 (-18.33-119.44)	92.78 (-6.09-333.84)	7.20
Forest		27.44 (-17.82-152.86)	89.04 (-6.78-349.44)	12.33
	5%	27.52 (-18.01-142.06)	91.29 (-5.00-302.79)	11.72
	10%	27.52 (-18.01-142.06)	91.29 (-5.00-302.79)	11.72
	15%	29.41 (-17.86-134.58)	88.87 (-5.26-364.52)	11.08
	30%	28.40 (-17.88-146.67)	90.04 (-6.97-310.13)	12.05
	pre-MTR	32.84 (-18.24-147.68)	95.00 (-6.41-329.85)	7.39

Table 6. LAI, albedo, and emissivity for all five areas. These include the increased elevation simulation (pre-MTR) and simulations based on increased area for the respective land-cover.

Composite		LAI	α	ε
Control		3.19	0.16	0.93
	pre-MTR	3.19	0.16	0.93
Bare Soil		1.60	0.27	0.92
	5%	1.60	0.27	0.92
	10%	1.60	0.27	0.92
	15%	1.59	0.27	0.92
	30%	1.58	0.27	0.92
	pre-MTR	1.60	0.27	0.92
Grass		2.91	0.18	0.94
	5%	2.91	0.18	0.94
	10%	2.91	0.18	0.94
	15%	2.91	0.18	0.94
	30%	2.91	0.18	0.94
	pre-MTR	2.91	0.18	0.94
Forest		3.16	0.16	0.93
	5%	3.16	0.16	0.93
	10%	3.16	0.16	0.93
	15%	3.16	0.16	0.93
	30%	3.16	0.16	0.93
	pre-MTR	3.16	0.16	0.93

Table 7. LCL, LFC, CAPE, and CIN for all five areas over 24 hours. These include the increased elevation simulation (pre-MTR) and simulations based on increased area for the respective land-cover.

Composite		LCL (m)	LFC (m)	CAPE (Jkg^{-1})	CIN (Jkg^{-1})
Control		563	1178	394	14
	pre-MTR	588	1187	410	13
Bare Soil		576	1063	459	12
	5%	604	1125	437	13
	10%	571	1036	458	11
	15%	590	1106	430	12
	30%	575	1069	447	11
	pre-MTR	570	1140	411	13
Grass		555	1118	430	13
	5%	563	1126	428	12
	10%	589	1110	449	11
	15%	569	1149	402	13
	30%	575	1199	419	13
	pre-MTR	532	1076	458	13
Forest		572	1142	422	13
	5%	586	1193	388	15
	10%	586	1193	388	15
	15%	601	1134	434	12
	30%	555	1113	428	14
	pre-MTR	575	1199	389	12